

⁵⁶Ni production in long-lived binary neutron star merger remnants

Maximilian Jacobi,^{1,*} Fabio Magistrelli,¹ Eleonora Loffredo,² Giacomo Ricigliano,³
Leonardo Chiesa,^{4,5} Sebastiano Bernuzzi,¹ Albino Perego,^{4,5} and Almudena Arcones^{3,6,7}

¹*Theoretisch-Physikalisches Institut, Friedrich-Schiller-Universität Jena, 07743, Jena, Germany*

²*INAF - Osservatorio Astronomico d'Abruzzo, Via M. Maggini snc, 64100 Teramo, Italy*

³*Institut für Kernphysik, Technische Universität Darmstadt, Schlossgartenstr. 2, Darmstadt 64289, Germany*

⁴*Dipartimento di Fisica, Università di Trento, Via Sommarive 14, 38123 Trento, Italy*

⁵*INFN-TIFPA, Trento Institute for Fundamental Physics and Applications, via Sommarive 14, I-38123 Trento, Italy*

⁶*GSI Helmholtzzentrum für Schwerionenforschung GmbH, Planckstr. 1, Darmstadt 64291, Germany*

⁷*Max-Planck-Institut für Kernphysik, Saupfercheckweg 1, Heidelberg 69117, Germany*

(Dated: March 25, 2025)

We investigate the nucleosynthesis and kilonova emission based on numerical-relativity binary neutron star merger simulations that incorporate a two-moment neutrino-transport scheme. Unlike in previous works with simpler neutrino treatments, a massive, fast (up to $v = 0.3c$), proton-rich neutrino-driven wind develops in the post-merger phase of the simulations as long as the merger remnant does not collapse to a black hole. We evolve the ejecta for 100 days after the merger using 2D ray-by-ray radiation-hydrodynamics simulations coupled in-situ to a complete nuclear network. The most abundant nucleosynthesis products are He, ⁵⁶Ni, and ⁵⁶Co. We find a total yield of $\sim 10^{-3}M_{\odot}$ of ⁵⁶Ni for all mergers that produce massive neutron star remnants, independently of the mass ratio and equation of state. After a few days, the decay of ⁵⁶Ni and later ⁵⁶Co becomes the primary source of heating in the matter expanding above the remnant. As a result, the kilonova light curve flattens on timescales of days for polar observation angles. The observation of this effect could serve as smoking gun for the presence of a long-lived neutron star remnant in future kilonova observations.

Introduction.—The mergers of binary neutron star (BNS) systems produce hot and dense ejecta, in which heavy elements are synthesized by the r -process [1–3]. During the expansion of the ejecta, heat generated by the radioactive decay of the newly formed heavy elements powers a fast transient, the kilonova (KN) [4, 5]. The combined heating of many r -process nuclei decaying simultaneously typically leads to a power-law like heating rate $\propto t^{-\alpha}$ with $\alpha \approx 1.1 - 1.4$ (see, *e.g.*, [5, 6]). Investigations of the KN AT2017gfo found a good agreement of the light curve with radioactive heating from r -process nuclei [7–12]. This is broadly consistent with simulations that find dynamical ejecta are typically at least mildly neutron-rich [13–17], although the ejected mass is insufficient to explain the luminosity and no ab-initio simulation can yet quantitatively reproduce the light curves.

Tens to hundreds of milliseconds after the merger, spiral-wave [16, 18] and neutrino-driven winds [19–22] can launch $\gtrsim 10^{-3}M_{\odot}$ of ejecta from the remnant accretion disk as long as the remnant does not collapse to a black hole (BH) shortly after the merger. Recent long-term BNS merger simulations presented in Just *et al.* [23], Radice and Bernuzzi [24], and Bernuzzi *et al.* [25] have found that a large fraction of the neutrino-driven wind exhibits electron-fractions close to 0.5. These simulations employ a two-moment “M1” neutrino-transport scheme, unlike previous long-time simulations of BNS mergers, which typically use a more approximate leakage-based neutrino transport [16, 17, 26]. As a consequence of the relatively high electron fraction, the nucleosynthesis in the neutrino-driven wind is dominated by an α -rich

freeze out and by the production of ⁵⁶Ni. In contrast to r -process powered transients, the heating rate in the proton-rich wind ejecta follows the exponential decay of ⁵⁶Ni and ⁵⁶Co with half-lives of 6 and 77 days, respectively. If a large enough amount of ⁵⁶Ni is produced in the neutrino-driven ejecta from BNS mergers, this could observably alter the associated KN light-curve compared to what would be expected from purely neutron-rich ejecta. Just *et al.* [23] find that iron-group elements are produced in the neutrino-driven wind. However, they do not find a significant enhancement of the KN luminosity. While it was confirmed that the decay of ⁵⁶Ni alone cannot account for the transient observed in 2017 [11], to our knowledge it has not been investigated whether the combined heating from ⁵⁶Ni and r -process elements are compatible with AT2017gfo.

In this work, we investigate the production of ⁵⁶Ni in neutrino-driven ejecta from BNS mergers and the impact on the KN emission based on the simulations presented in Radice and Bernuzzi [24], Bernuzzi *et al.* [25], and Gutiérrez *et al.* [27].

Methods.—We analyze and compare the ejection of proton-rich material in four numerical relativity (NR) BNS merger simulations summarized in table I. They consist of two asymmetric ($q > 1$), BLh_q1.49 and DD2_q1.77, and two symmetric ($q = 1$) BNS systems, SFHo_q1.0 and DD2_q1.0, employing three different microphysical equations of state (EOSs): SFHo [28], DD2 [29, 30], and BLh [31, 32]. All models discussed in this work have been presented in previous publications [24, 25, 27]. Note, that we use the baryon-mass ratio

TABLE I. Overview of the BNS models considered in this work. Given are initial gravitational BNS masses, the simulated post-merger time, the time of BH formation after merger, the total ejecta mass, the mass of r -process ejecta ($Y_e < 0.25$), and proton-rich ejecta ($Y_e > 0.5$) and the total mass of ejected He and ^{56}Ni $M_{\text{ej}}^{\text{He}}$, $M_{\text{ej}}^{\text{Ni}}$, respectively.

Model	M_1	M_2	t_{pm}	t_{BH}	M_{ej}	M_{ej}^r	M_{ej}^p	$M_{\text{ej}}^{\text{He}}$	$M_{\text{ej}}^{\text{Ni}}$
	[M_{\odot}]		[ms]						
BLh_q1.49	1.64	1.15	103	114	10.85	4.01	3.72	3.03	0.84
DD2_q1.77	1.81	1.08	111	-	25.31	19.30	1.59	1.56	0.43
DD2_q1.0	1.35	1.35	79	-	5.80	1.18	1.53	1.23	0.41
SFHo_q1.0	1.35	1.35	35	5.7	6.25	3.51	0.00	0.09	0.01

$q = M_1^{\text{b}}/M_2^{\text{b}} \geq 1$ for the naming of models to stay consistent with the naming convention in Bernuzzi *et al.* [25] while table I lists the gravitational masses M_1, M_2 .

All simulations are performed with the THC code [33–38], which is built on top of the Cactus framework [39, 40]. The simulations employ a truncated, two-moment gray neutrino-transport scheme that retains all nonlinear neutrino-matter coupling terms [38] and uses the Minerbo closure. The set of weak reactions included in the transport scheme is described in *e.g.* [37, 41, 42]. The general-relativistic hydrodynamics equations are formulated in conservative form (see [15] for details on the precise equations solved here) and augmented by a large-eddy-scheme that accounts for angular momentum transport due to magnetohydrodynamical effects [24, 43, 44].

The equal-mass simulations, DD2_q1.0 and SFHo_q1.0, consist of two $1.35M_{\odot}$ neutron stars. In the BLh_q1.49 model, the BNS masses are compatible with the chirp mass measured in GW170817 and the mass ratio lies at the upper bound of the constraints inferred with low spin priors [45]. The DD2_q1.77 model exhibits an even larger mass ratio, and as such represents a comparably extreme case. Of the 4 binaries considered in this work, only the remnant in SFHo_q1.0 collapses to a BH in the gravitational-wave driven phase of the dynamics, while the central remnant is a massive neutron star for the duration of the simulation in the other 3 models. These models eject matter for the full duration of the simulations until ~ 100 ms post merger. Model BLh_q1.49 collapses 114 ms post-merger (*i.e.*, shortly after the ejecta analyzed in this work were extracted).

We evolve the ejecta and the nucleosynthesis during the expansion up to $t = 100$ d with the Lagrangian radiation-hydrodynamics code SNEC [46, 47] coupled to the SkyNet nuclear network [48], as described in [49, 50]. We construct axisymmetric Lagrangian initial data for the SNEC simulations from the ejecta properties extracted from the 3D simulations presented above by averaging over the azimuthal angle at a fixed radius of ~ 450 km as described in [47]. The dependency on the polar angle of

the ejecta properties is approximately included in a ray-by-ray fashion by mapping the initial profile into an effective 1D problem for a number of angular bins. One full simulation includes 26 rays uniformly spaced in the polar angle ranging from $\theta = 0$ (polar) to $\theta = \pi/2$ (equatorial) assuming mirror symmetry across the equatorial plane. To ensure that all the intensive quantities (including the density) remain unaltered, we multiply the total mass by the scaling factor $\lambda_{\theta} = 4\pi/\Delta\Omega$, where $\Delta\Omega \simeq 2\pi \sin\theta d\theta$ is the solid angle of the angular bin. Each angular section is discretized radially into 1000 fluid elements and evolved independently (non-radial flow of matter and photons is neglected) up to $t = 100$ d. We note that the ejecta velocities change by up to a few percent of the speed of light after the transition from the THC to the SNEC simulations. This is likely caused by the method of initialization of the SNEC simulations (see [47]), the transition from a general relativistic to a Newtonian description of gravity, and the switch of the employed EOSs. This change in velocity likely has a small impact on the predicted KN light curve but we do not expect it to affect the conclusions drawn in this paper.

The nuclear network includes 7836 isotopes up to ^{337}Cn and uses the JINA REACLIB [51] and the same setup as in [52, 53]. We self-consistently couple the effects of nuclear heating from the in-situ network with the hydrodynamics evolution. The thermalization of energy produced by nuclear reactions is treated explicitly for contributions from γ rays, α particles, electrons, and other nuclear reactions products and is described in detail in [49]. For some ejecta components, the temperature at the moment of mapping has already dropped below ~ 6 GK. To ensure consistent initialization in nuclear statistical equilibrium (NSE) conditions, we extrapolate to earlier times using an analytic trajectory starting at $T = 8$ GK as described in [50]. To calculate the luminosity in each angular section, we employ the analytic, time-independent opacity described in [47]. The KN light curves are then combined for different viewing angles as described in [21, 54].

KN spectra from each angular section are computed using the radiative transfer spectral synthesis code TARDIS [55]. The density, velocity, and composition profiles are obtained by rebinning the fluid elements outside the photosphere into 50 radial shells, while the input luminosity is given by the bolometric luminosity, $L = \sum_{\theta} L_{\theta}/\lambda_{\theta}$ where L_{θ} are the luminosities from the individual rays. We use the atomic dataset developed by Gillanders *et al.* [56], considering atomic lines up to Zr III. Ionization and excitation are treated with the local thermal equilibrium and dilute local thermal equilibrium approximations, respectively, while the “macroatom” scheme is employed for line interaction treatment. In addition to KN spectra obtained from each ray, we combine them for fixed viewing angle following the same weighting prescription used for the luminosity computed in the SNEC simulations.

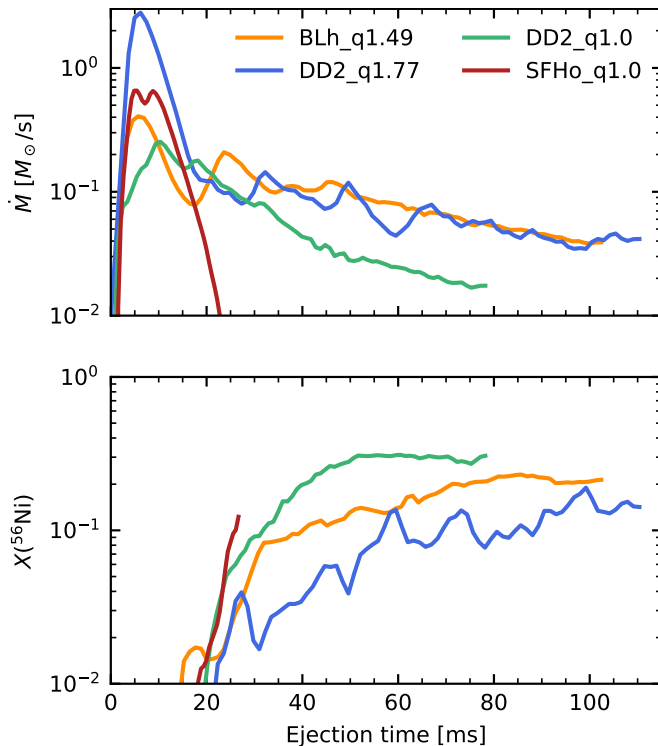


FIG. 1. Top panel: mass-ejection rate for the considered BNS models. Bottom panel: ^{56}Ni mass fraction of the ejecta $X(^{56}\text{Ni}) = \frac{\dot{M}_{\text{Ni}}}{\dot{M}_{\text{tot}}}$ after 10 days. The x -axis shows the time of ejection defined as the time at which the fluid elements cross the sphere at ~ 450 km.

Results.— The upper panel of fig. 1 shows the mass ejection rate as a function of ejection time for the 4 models considered in this work. Here “ejection time” refers to the time at which matter crosses the sphere at ~ 450 km and is therefore slightly delayed with respect to the actual time of ejection from the merger remnant. All models exhibit dynamical ejecta of tidal and shock-heated origin within the first 10 ms after merger. After that, oscillations of the massive neutron star drive a spiral-wave wind that ejects moderately neutron-rich matter leading to an oscillatory mass ejection rate. This ejection continues until the end of the simulation or the collapse of the remnant. Such a spiral-wave wind is stronger in the asymmetric models, especially in DD2_q1.77, where it persists until the end of the simulation.

The neutrino-driven mass ejection starts ~ 10 ms after the merger in the polar direction ($\theta \lesssim 30^\circ$) and continues until the end of the simulation or the collapse of the remnant. In the almost exclusively proton-rich polar ejecta, the freeze-out from NSE is dominated by α -particles resulting in a final He mass fraction of $\sim 10\%$ in agreement with the values found in Just *et al.* [23]. This could lead to a detectable feature in the KN spectrum after a few days [53, 57] indicating the presence of a long-lived neutron-star remnant [58].

Furthermore, α -captures synthesize nuclei along the $Z = N$ line on the nuclear chart ending at ^{56}Ni due to its doubly magic nature. The lower panel of fig. 1 shows the ^{56}Ni mass fraction of the ejected fluid elements after 10 s ($X(^{56}\text{Ni}) = \dot{M}_{\text{Ni}}/\dot{M}_{\text{tot}}$) as function of their ejection time. In the non-collapsing models, the mass fraction of ^{56}Ni reaches $\sim 10 - 30\%$ and increases with time as the neutrino-driven wind becomes more proton-rich. DD2_q1.77 exhibits a comparably low mass fraction due to its long-lasting spiral-wave wind ejecta component which ejects slightly neutrino-rich matter alongside the polar proton-rich wind, thereby lowering the relative fraction of ^{56}Ni . We also observe the beginning of a neutrino-driven wind and the production of ^{56}Ni in SFHo_q1.0 but due to its early collapse the overall mass is much smaller than in the non-collapsing models and therefore negligible.

Note that a neutrino-driven wind is also present in previous BNS merger simulations using leakage scheme and “M0” neutrino absorption scheme [15, 16, 26]. The crucial difference is that the M1 neutrino transport scheme leads to a more massive and more proton-rich wind. In the M0 neutrino scheme, neutrinos are only transported in a radial ray-by-ray fashion. The region with the highest neutrino emissivity, however, lies at the remnant-disk interface (*i.e.*, off-center). Thus, the neutrino-driven wind is not as massive and ejected closer to the equatorial plane in M0 simulations. In the M1 scheme however, neutrinos emitted from the disk interface can move vertically leading to a more massive neutrino-driven wind with a more polar ejection angle, as already visible in older simulations that did not prescribe radial neutrino fluxes [20].

Figure 2 shows the spatial distribution of the ejecta 1 day after merger for the BLh_q1.49 model. The top and bottom left quadrants show the spatial distribution of the initial electron fraction and entropy, respectively as extracted from the NR simulation. The tidal ejecta are located close to the equatorial plane with low electron fractions and entropies while the shock-heated ejecta are more spread and exhibit a large range in electron fraction and entropy. In the asymmetric models, the tidal ejecta are more massive than the shock-heated ejecta (in DD2_q1.77, the tidal ejecta contribute $\sim 50\%$ of the total ejecta mass), while the shock heated ejecta are more important in the equal-mass models.

If the initial electron fraction of the ejecta is even slightly neutron-rich, the small amount of free neutrons drive the composition away from the $Z = N$ line and toward the valley of stability. To produce ^{56}Ni , the electron fraction must therefore be fairly high ($Y_e \gtrsim 0.48$). This condition leads to a sharply bounded region where the ^{56}Ni mass fractions lie between 1% and 30% as visible in the top right quadrant in fig. 2 showing the mass fraction of ^{56}Ni after 1 day. Higher entropies disfavor the formation of seed nuclei from α particles leading to

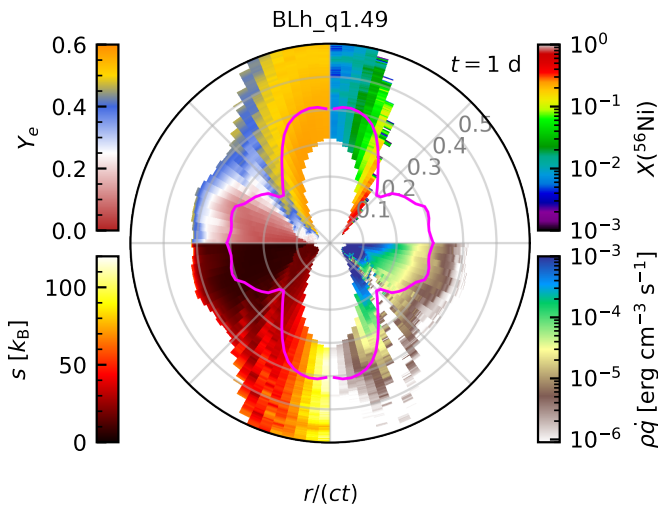


FIG. 2. Spatial distribution of the ejecta of the BLh.q1.49 model after 1 day. Top-left quadrant: electron fraction at the beginning of the SNEC simulation. Top-right quadrant: mass fraction of ^{56}Ni . Bottom-left quadrant: initial entropy at the beginning of the SNEC simulation. Bottom-right quadrant: local heating rate. The magenta line indicates the position of the photosphere. Regions with $Y_e \gtrsim 0.48$ and $s \lesssim 50k_B/\text{baryon}$ produce a large amount of ^{56}Ni which has a significant impact on the heating rate on the timescale of days.

less effective production of ^{56}Ni and a higher He mass fraction. Therefore, the ^{56}Ni mass fraction decreases for angles close to the polar axis. The high entropy ejecta could potentially host a νp process [59–63]. However, our network calculations do not include neutrino capture reactions and can therefore not capture the νp -process.

The overall ejecta masses, the mass of ejecta hosting a strong r -process M_{ej}^r (which we approximate as the ejecta with $Y_e < 0.25$), proton-rich ejecta M_{ej}^p ($Y_e > 0.5$), He, and ^{56}Ni are reported in table I. The mass of proton-rich ejecta exceeds $10^{-3}M_\odot$ in all non-collapsing models and is highest in BLh.q1.49. In the proton-rich ejecta, the ^{56}Ni mass fraction is approximately $\sim 22 - 27\%$. At the end of the simulations employing the DD2 EOS, the neutrino-driven wind is still ejecting matter with high electron fraction. The ^{56}Ni masses reported in table I as well as the results that follow from it should therefore be considered lower limits in these models.

The lower right quadrant in fig. 2 shows the local heating rate at $t = 1$ d in the BLh.q1.49 model. There are two distinct regions visible. In the neutron-rich equatorial region, the decay of r -process material dominates, while the decay of ^{56}Ni is almost exclusively responsible for the nuclear energy generation in the polar region. At one day (roughly when the photosphere starts to enter the bulk of the ejecta), the energy generation in the two regions is already comparable. Figure 3 shows nuclear energy generation and luminosities for the 4 simulations

considered in this work. Solid lines in the left panel show the mass-averaged specific energy generation \dot{q} due to the decay of ^{56}Ni and ^{56}Co , dashed lines show the combined contribution of all other isotopes, and thin lines show the total. In BLh.q1.49 and DD2.q1.0, the energy generated by the decay of ^{56}Ni makes up more than 50% of the total heating after 3 days and more than 75% after 10 days.

Due to the large tidal ejecta mass in DD2.q1.77 the relative contribution of ^{56}Ni is reduced, resulting in 10 (25)% after 3 (10) days. In all three models, the decay of ^{56}Co makes up the largest part of the total energy generated around 100 days. Since the heating rate follows the decay of two nuclei, it deviates significantly from the power-law behavior $\propto t^{-1.3}$ (shown as dotted black line) expected for the combined heating of r -process elements. The combined heating from all other decays (dashed lines) is reasonably well described by the power law. The slight bump at a few days is caused by the β decay of ^{132}I which is fed by the decay of ^{132}Te with a half-life of 3.2 days [64].

To estimate their contribution to the light curve, we separately calculate the thermalized heating rate of ^{56}Ni and ^{56}Co outside the photosphere. The middle panel of fig. 3 shows the bolometric luminosity for each of the simulations (solid lines). Similar to the left panel, solid lines show the contribution from the decay chain of ^{56}Ni outside the photosphere and dashed lines show the difference between the total luminosity (thin lines) and the ^{56}Ni and ^{56}Co contribution. Within the first 5 days the ^{56}Ni is partially hidden within the photosphere and its impact thus not yet visible. Furthermore, the impact of the ^{56}Ni heating on the bolometric light curve is smaller compared to its impact on the nuclear energy generation due to the fact that the energy of the decay is exclusively released in γ rays and neutrinos. Since the neutrino-driven ejecta become mostly transparent to γ rays within the first 5 to 10 days, the energy generated by ^{56}Ni does not thermalize effectively. In the equatorial region, on the other hand, the γ -ray opacities are higher and a large fraction of the energy generated by r -process nuclei is released by β -decay electrons which thermalize more efficiently. While ^{56}Co also decays primarily via electron capture, it can also β^+ decay, emitting on average 121 keV via positrons per decay [12]. Therefore, after $t \gtrsim 10$ d, the impact of ^{56}Co on the bolometric luminosity increases significantly. In DD2.q1.77, where the ratio of M_{ej}^r to $M_{\text{ej}}^{\text{Ni}}$ is very high (see table I), the heating from ^{56}Ni and ^{56}Co does not contribute significantly.

For a polar viewing angle, the neutrino-driven ejecta fill a large fraction of the field of view while the tidal ejecta are subdominant. Consequently, the contribution of ^{56}Ni and ^{56}Co to the observed luminosities is significantly enhanced and reaches 50% after 5 to 7 days for DD2.q1.0 and BLh.q1.49. In DD2.q1.77, the contribution of ^{56}Ni and ^{56}Co to the observed luminosity is still mostly overshadowed by the decay of r -process elements

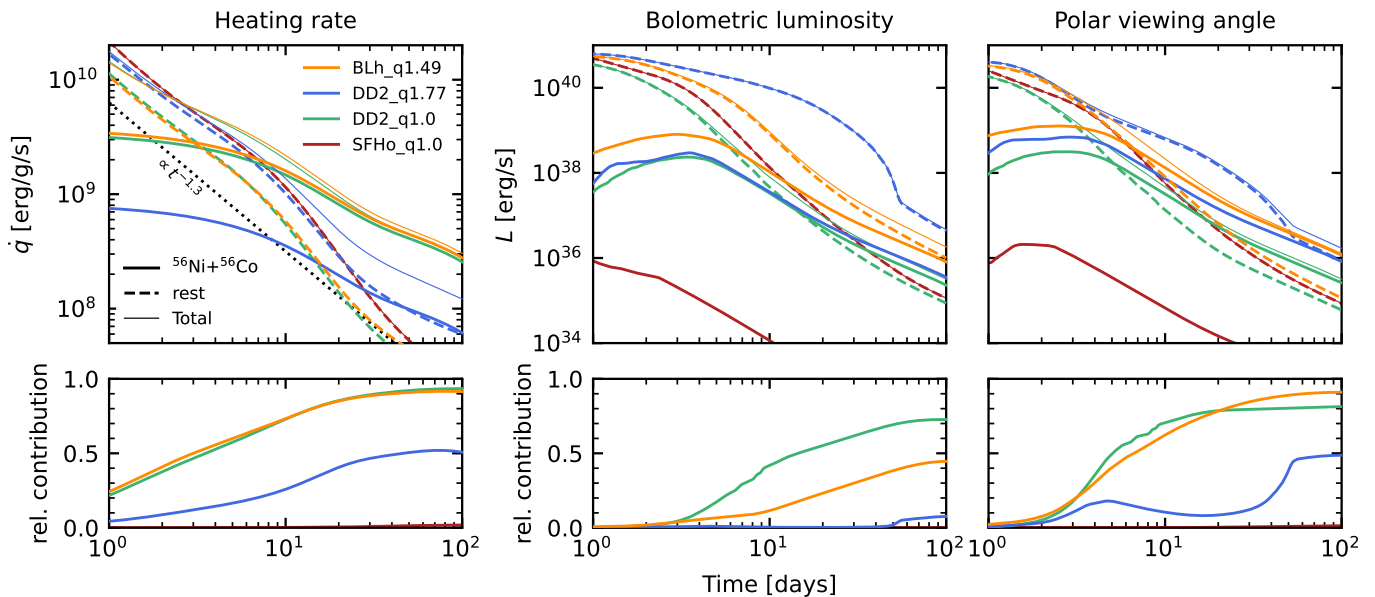


FIG. 3. Mass-averaged nuclear energy generation (left panels), bolometric luminosity (middle panels) and luminosity observed at a viewing angle 20° (right panels). The upper panels show the heating and luminosities generated by the decay of ^{56}Ni and ^{56}Co (solid lines), the contribution of all remaining isotopes (dashed lines), and the total (thin lines). The dotted black line in the upper left panel indicates a heating rate proportional to $t^{-1.3}$. The lower panels show the relative contribution of ^{56}Ni and ^{56}Co in each of the above panels.

where the most relevant isotopes are ^{132}I and later the α emitters ^{225}Ac which decays with a half-life of 10 days [64] and subsequently ^{221}Fr . After $t \gtrsim 50$ d, their decay becomes less important and at the same time α particles begin to thermalize less efficiently than electrons and positrons. Thus, at these late times the decay of ^{56}Co becomes more relevant again.

We calculate the EM spectra after $t = 1$ d for BLh_q1.49 with TARDIS using the ray-by-ray approach outlined above. The two most prominent features in the spectra are created by Sr and Ca [53, 65, 66]. Ca is primarily produced in the form of ^{48}Ca in the slightly neutron-rich part of the ejecta but $\sim 10\%$ is produced as ^{40}Ca in the proton-rich wind. Iron-group elements are not visible in the spectra due to the low luminosities at the relevant wavelengths ($\sim 4000 \text{ \AA}$) and the dominance of Ca and Sr lines. We thus cannot identify a direct indication of proton-rich ejecta in the early spectra.

Most of the γ rays emitted by the decay of ^{56}Ni and ^{56}Co escape the ejecta and thus contribute to the γ -ray spectrum. Previous works have investigated the possibility of direct detection of γ rays from the decay of r -process nuclei [67–69], however, they did not include the emission from iron-group elements. We calculate the γ -ray emission spectrum at $t = 7$ d for BLh_q1.49 accounting for the relativistic Doppler shift for each fluid element individually. The resulting spectrum is shown in fig. 4 for a face-on (upper panel) and an edge-on viewing angle (lower panel) assuming an event distance of 40 Mpc. The partial spectra from the most relevant isotopes are shown

by colored lines and the position of the corresponding unshifted emission lines are indicated by arrows above the panels. In the energy range between 100 keV and 10 MeV, both spectra are dominated by ^{56}Ni and ^{56}Co lines. From a face-on viewing angle, the wind ejecta are moving either away (below the merger remnant) or towards the observer (above the merger remnant). Lines from ^{56}Ni and ^{56}Co are thus either red or blue shifted and form a double-peak. γ rays from r -process elements stem mostly from the tidal ejecta in the equatorial plane resulting in narrower lines. For an edge-on observer, peaks from ^{56}Ni and ^{56}Co are instead narrower while those from r -process isotopes are broader. We also include the sensitivity curve of NuStar, the Compton Spectrometer and Imager (COSI) [70], e-ASTROGRAM [71], and GammaTPC [72]. Even though γ ray emissions from ^{56}Ni and ^{56}Co increase the peak flux by an order of magnitude, the detection with COSI would require an event within the very optimistic distance of ~ 5 Mpc while e-ASTROGRAM would require ~ 15 Mpc. However, GammaTPC would be sensitive enough to detect the double peak due to the decay of ^{56}Ni around 700 – 800 keV for an event at a distance of 40 Mpc.

Conclusion.—We analyzed the outflow of 4 long-term BNS merger simulations employing a state-of-the-art M1 neutrino transport scheme. All non-collapsing models eject large amounts of proton-rich ejecta ($\sim 10^{-3} M_\odot$) synthesizing $\sim 4 - 8 \times 10^{-4} M_\odot$ of ^{56}Ni , the decay of which can significantly alter the late ($t \gtrsim 5$ d) light curve. The observation of this effect in a KN would strongly indicate

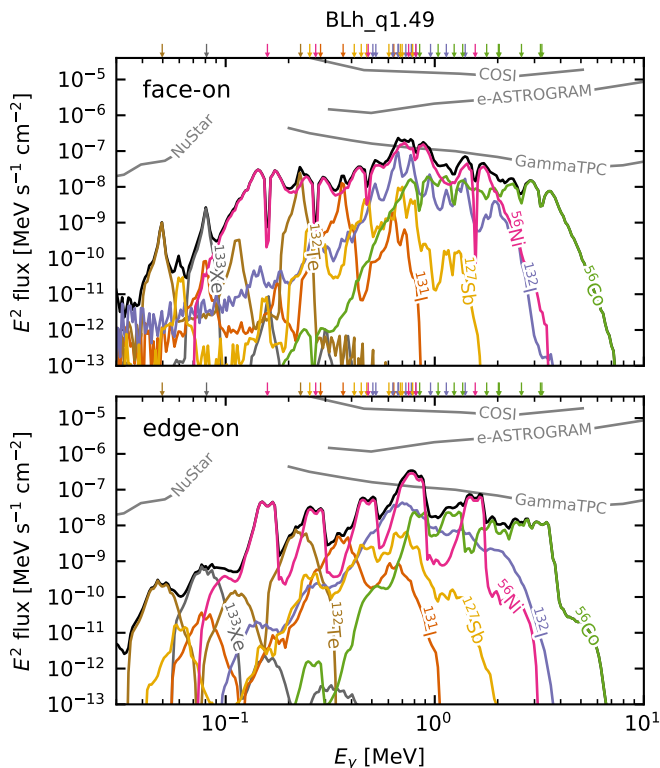


FIG. 4. γ -ray emission spectrum at $t = 7$ d for BLh_q1.49 at 40 Mpc for a face-on (upper panel) and an edge-on (lower panel) viewing angle. Colored lines and arrows on top of the panels indicate the contribution of individual isotopes and the original line positions, respectively. Gray lines show the sensitivity of the NuStar, COSI, e-ASTROGRAM, and GammaTPC telescopes.

that the remnant of the BNS merger did not collapse to a BH for at least ~ 100 ms after the merger. Due to the uncertainty involved in inferring the bolometric light curve based on the observation of AT2017gfo (*e.g.*, [8]) and the thermalization of nuclear heating, it is unclear whether the observation is consistent with the presence of ^{56}Ni . The latter could be instead verified in the nebular-phase spectrum. Given the strong asymmetry in the ejecta composition, the very high relative amount of ^{56}Ni ($\sim 20 - 30\%$) in the proton rich ejecta could lead to the presence of strong ^{56}Ni and ^{56}Co features on a timescale of weeks, possibly in the wavelength range $\sim 7000 - 7500 \text{ \AA}$ [73]. However, a consistent modeling of the ionization structure would be needed in order to predict the overall and relative strengths of such features [74].

For a confirmation of our results, more work will be needed in the future. Future magnetohydrodynamics simulation including a sophisticated neutrino transport scheme will be necessary since magnetic fields might launch magnetically-driven winds on similar timescales to the neutrino-driven wind [17, 26]. This could reduce the electron fraction of the ejecta and thus suppress the

proton-rich ejecta. The recent work by Musolino *et al.* [75] presents BNS merger simulations including both an M1 neutrino transport and magnetic fields. While their figure 2 indicates the presence of some proton-rich ejecta, they do not provide quantitative information about the composition of the ejected material. Furthermore, the neutrino transport employed in our 3D simulations, while being state-of-the-art (especially for long simulations), is only approximate. Future studies with an energy dependent neutrino transport scheme and more accurate set of weak reactions will be needed to confirm the presence of proton-rich neutrino-driven winds from BNS merger remnants. While the presence of iron-group elements has a clear impact on the nuclear energy generation, uncertainties in the thermalization efficiency complicate the quantitative characterization of the effect on the light curve. Nonetheless, the presence of ^{56}Ni in the ejecta can have a significant effect on the KN emission, especially on the timescale of 10 - 100 days. Thus, our work suggests that future parametric studies of KNe should include the possibility for the presence of iron-group elements.

We would like to thank David Radice for providing simulation data, James Gillanders for providing atomic data for TARDIS and Oliver Just, Kenta Hotokezaka, and Moritz Reichert for fruitful discussions and comments. SB and MJ acknowledge support by the EU Horizon under ERC Consolidator Grant, no. InspiReM-101043372. FM acknowledges support from the Deutsche Forschungsgemeinschaft (DFG) under Grant No.406116891 within the Research Training Group RTG 2522/1. GR and AA acknowledge support from the Deutsche Forschungsgemeinschaft (DFG, German Research Foundation, Project ID 279384907, SFB 1245) and the State of Hesse within the Research Cluster ELEMENTS (Project ID 500/10.006). EL acknowledges support by the European Union – NextGenerationEU RFF M4C2 1.1 PRIN 2022 project 2022RJLWHN URKA. The work of AP is partially funded by the European Union - Next Generation EU, Mission 4 Component 2 - CUP E53D23002090006 (PRIN 2022 Prot. No. 2022KX2Z3B).

Simulations were performed on SuperMUC-NG at the Leibniz-Rechenzentrum (LRZ) Munich and on the national HPE Apollo Hawk at the High Performance Computing Center Stuttgart (HLRS). The authors acknowledge the Gauss Centre for Supercomputing e.V. (www.gauss-centre.eu) for funding this project by providing computing time on the GCS Supercomputer SuperMUC-NG at LRZ (allocations pn36ge, pn36jo and pn68wi). The authors acknowledge HLRS for funding this project by providing access to the supercomputer HPE Apollo Hawk under the grant number INTRHYGUE/44215 and MAGNETIST/44288. Post-processing and development runs were performed on the ARA cluster at Friedrich

Schiller University Jena. The ARA cluster is funded in part by DFG grants INST 275/334-1 FUGG and INST 275/363-1 FUGG, and ERC Starting Grant, grant agreement no. BinGraSp-714626.

* maximilian.jacobi@uni-jena.de

- [1] E. Symbalisty and D. N. Schramm, Neutron star collisions and the r-process, *Astrophys. J. Lett.* **22**, 143 (1982).
- [2] D. Eichler, M. Livio, T. Piran, and D. N. Schramm, Nucleosynthesis, Neutrino Bursts and Gamma-Rays from Coalescing Neutron Stars, *Nature* **340**, 126 (1989).
- [3] C. Freiburghaus, S. Rosswog, and F. K. Thielemann, R-Process in Neutron Star Mergers, *Astrophys. J.* **525**, L121 (1999).
- [4] L.-X. Li and B. Paczynski, Transient events from neutron star mergers, *Astrophys. J. Lett.* **507**, L59 (1998).
- [5] B. D. Metzger, G. Martinez-Pinedo, S. Darbha, E. Quataert, A. Arcones, D. Kasen, R. Thomas, P. Nugent, I. V. Panov, and N. T. Zinner, Electromagnetic Counterparts of Compact Object Mergers Powered by the Radioactive Decay of R-process Nuclei, *Mon. Not. Roy. Astron. Soc.* **406**, 2650 (2010).
- [6] O. Korobkin, S. Rosswog, A. Arcones, and C. Winteler, On the astrophysical robustness of neutron star merger r-process, *Mon. Not. Roy. Astron. Soc.* **426**, 1940 (2012).
- [7] S. Tanaka (AXEL), Development of the front-end board of a Xenon gas Time Projection Chamber at the AXEL neutrinoless double beta decay search experiment, *J. Phys. Conf. Ser.* **888**, 012075 (2017).
- [8] E. Waxman, E. O. Ofek, D. Kushnir, and A. Gal-Yam, Constraints on the ejecta of the GW170817 neutron-star merger from its electromagnetic emission, *Mon. Not. Roy. Astron. Soc.* **481**, 3423 (2018).
- [9] M. M. Kasliwal *et al.*, Illuminating Gravitational Waves: A Concordant Picture of Photons from a Neutron Star Merger, *Science* **358**, 1559 (2017).
- [10] A. Murguia-Berthier *et al.*, A Neutron Star Binary Merger Model for GW170817/GRB 170817A/SSS17a, *Astrophys. J. Lett.* **848**, L34 (2017).
- [11] P. S. Cowperthwaite *et al.*, The Electromagnetic Counterpart of the Binary Neutron Star Merger LIGO/Virgo GW170817. II. UV, Optical, and Near-infrared Light Curves and Comparison to Kilonova Models, *Astrophys. J. Lett.* **848**, L17 (2017).
- [12] M.-R. Wu, J. Barnes, G. Martinez-Pinedo, and B. D. Metzger, Fingerprints of heavy element nucleosynthesis in the late-time lightcurves of kilonovae, *Phys. Rev. Lett.* **122**, 062701 (2019).
- [13] S. Rosswog, M. Liebendoerfer, F. K. Thielemann, M. B. Davies, W. Benz, and T. Piran, Mass ejection in neutron star mergers, *Astron. Astrophys.* **341**, 499 (1999).
- [14] K. Hotokezaka, K. Kiuchi, K. Kyutoku, T. Muranushi, Y.-i. Sekiguchi, M. Shibata, and K. Taniguchi, Remnant massive neutron stars of binary neutron star mergers: Evolution process and gravitational waveform, *Phys. Rev. D* **88**, 044026 (2013).
- [15] D. Radice, A. Perego, K. Hotokezaka, S. A. Fromm, S. Bernuzzi, and L. F. Roberts, Binary Neutron Star Mergers: Mass Ejection, Electromagnetic Counterparts and Nucleosynthesis, *Astrophys. J.* **869**, 130 (2018).
- [16] V. Nedora, S. Bernuzzi, D. Radice, B. Daszuta, A. Endrizzi, A. Perego, A. Prakash, M. Safarzadeh, F. Sichi-anchi, and D. Logoteta, Numerical Relativity Simulations of the Neutron Star Merger GW170817: Long-Term Remnant Evolutions, Winds, Remnant Disks, and Nucleosynthesis, *Astrophys. J.* **906**, 98 (2021).
- [17] K. Kiuchi, S. Fujibayashi, K. Hayashi, K. Kyutoku, Y. Sekiguchi, and M. Shibata, Self-Consistent Picture of the Mass Ejection from a One Second Long Binary Neutron Star Merger Leaving a Short-Lived Remnant in a General-Relativistic Neutrino-Radiation Magneto-hydrodynamic Simulation, *Phys. Rev. Lett.* **131**, 011401 (2023).
- [18] V. Nedora, S. Bernuzzi, D. Radice, A. Perego, A. Endrizzi, and N. Ortiz, Spiral-wave wind for the blue kilonova, *Astrophys. J. Lett.* **886**, L30 (2019).
- [19] L. Dessart, C. D. Ott, A. Burrows, S. Rosswog, and E. Livne, Neutrino signatures and the neutrino-driven wind in Binary Neutron Star Mergers, *Astrophys. J.* **690**, 1681 (2009).
- [20] A. Perego, S. Rosswog, R. M. Cabezón, O. Korobkin, R. Käppeli, A. Arcones, and M. Liebendörfer, Neutrino-driven winds from neutron star merger remnants, *Mon. Not. Roy. Astron. Soc.* **443**, 3134 (2014).
- [21] D. Martin, A. Perego, A. Arcones, F.-K. Thielemann, O. Korobkin, and S. Rosswog, Neutrino-driven winds in the aftermath of a neutron star merger: nucleosynthesis and electromagnetic transients, *Astrophys. J.* **813**, 2 (2015).
- [22] S. Fujibayashi, M. Shibata, S. Wanajo, K. Kiuchi, K. Kyutoku, and Y. Sekiguchi, Mass ejection from disks surrounding a low-mass black hole: Viscous neutrino-radiation hydrodynamics simulation in full general relativity, *Phys. Rev. D* **101**, 083029 (2020).
- [23] O. Just, V. Vijayan, Z. Xiong, S. Goriely, T. Soultanis, A. Bauswein, J. Guilet, H. T. Janka, H.-T. Janka, and G. Martinez-Pinedo, End-to-end Kilonova Models of Neutron Star Mergers with Delayed Black Hole Formation, *Astrophys. J. Lett.* **951**, L12 (2023).
- [24] D. Radice and S. Bernuzzi, Ab-initio General-relativistic Neutrino-radiation Hydrodynamics Simulations of Long-lived Neutron Star Merger Remnants to Neutrino Cooling Timescales, *Astrophys. J.* **959**, 46 (2023).
- [25] S. Bernuzzi, F. Magistrelli, M. Jacobi, D. Logoteta, A. Perego, and D. Radice, Long-lived neutron-star remnants from asymmetric binary neutron star mergers: element formation, kilonova signals and gravitational waves, [arXiv:2409.18185 \[astro-ph.HE\]](https://arxiv.org/abs/2409.18185) (2024).
- [26] L. Combi and D. M. Siegel, GRMHD Simulations of Neutron-star Mergers with Weak Interactions: r-process Nucleosynthesis and Electromagnetic Signatures of Dynamical Ejecta, *Astrophys. J.* **944**, 28 (2023).
- [27] E. M. Gutiérrez, M. Bhattacharya, D. Radice, K. Murase, and S. Bernuzzi, Cocoon shock breakout emission from binary neutron star mergers, [arXiv:2408.15973 \[astro-ph.HE\]](https://arxiv.org/abs/2408.15973) (2024).
- [28] A. W. Steiner, M. Hempel, and T. Fischer, Core-collapse supernova equations of state based on neutron star observations, *Astrophys. J.* **774**, 17 (2013).
- [29] S. Typel, G. Ropke, T. Klahn, D. Blaschke, and H. H. Wolter, Composition and thermodynamics of nuclear matter with light clusters, *Phys. Rev. C* **81**, 015803 (2010).

- [30] M. Hempel and J. Schaffner-Bielich, Statistical Model for a Complete Supernova Equation of State, *Nucl. Phys. A* **837**, 210 (2010).
- [31] I. Bombaci and D. Logoteta, Equation of state of dense nuclear matter and neutron star structure from nuclear chiral interactions, *Astron. Astrophys.* **609**, A128 (2018).
- [32] D. Logoteta, A. Perego, and I. Bombaci, Microscopic equation of state of hot nuclear matter for numerical relativity simulations, *Astron. Astrophys.* **646**, A55 (2021).
- [33] D. Radice and L. Rezzolla, THC: a new high-order finite-difference high-resolution shock-capturing code for special-relativistic hydrodynamics, *Astron. Astrophys.* **547**, A26 (2012).
- [34] D. Radice, L. Rezzolla, and F. Galeazzi, Beyond second-order convergence in simulations of binary neutron stars in full general-relativity, *Mon. Not. Roy. Astron. Soc.* **437**, L46 (2014).
- [35] D. Radice, L. Rezzolla, and F. Galeazzi, High-Order Numerical-Relativity Simulations of Binary Neutron Stars, *ASP Conf. Ser.* **498**, 121 (2015).
- [36] D. Radice, L. Rezzolla, and F. Galeazzi, High-Order Fully General-Relativistic Hydrodynamics: new Approaches and Tests, *Class. Quant. Grav.* **31**, 075012 (2014).
- [37] D. Radice, F. Galeazzi, J. Lippuner, L. F. Roberts, C. D. Ott, and L. Rezzolla, Dynamical Mass Ejection from Binary Neutron Star Mergers, *Mon. Not. Roy. Astron. Soc.* **460**, 3255 (2016).
- [38] D. Radice, S. Bernuzzi, A. Perego, and R. Haas, A new moment-based general-relativistic neutrino-radiation transport code: Methods and first applications to neutron star mergers, *Mon. Not. Roy. Astron. Soc.* **512**, 1499 (2022).
- [39] T. Goodale, G. Allen, G. Lanfermann, J. Massó, T. Radke, E. Seidel, and J. Shalf, The Cactus Framework and Toolkit: Design and Applications, in *VECPAR 2002*, Vol. 2565 (Springer Berlin Heidelberg, 2003) pp. 197–227.
- [40] E. Schnetter, C. D. Ott, G. Allen, P. Diener, T. Goodale, T. Radke, E. Seidel, and J. Shalf, Cactus Framework: Black Holes to Gamma Ray Bursts, [arXiv:0707.1607 \[cs.DC\]](https://arxiv.org/abs/0707.1607) (2007).
- [41] F. Galeazzi, W. Kastaun, L. Rezzolla, and J. A. Font, Implementation of a simplified approach to radiative transfer in general relativity, *Phys. Rev. D* **88**, 064009 (2013).
- [42] A. Perego, S. Bernuzzi, and D. Radice, Thermodynamics conditions of matter in neutron star mergers, *Eur. Phys. J. A* **55**, 124 (2019).
- [43] D. Radice, General-Relativistic Large-Eddy Simulations of Binary Neutron Star Mergers, *Astrophys. J. Lett.* **838**, L2 (2017).
- [44] D. Radice, Binary Neutron Star Merger Simulations with a Calibrated Turbulence Model, *Symmetry* **12**, 1249 (2020).
- [45] B. P. Abbott *et al.* (LIGO Scientific, Virgo), Properties of the binary neutron star merger GW170817, *Phys. Rev. X* **9**, 011001 (2019).
- [46] V. Morozova, A. L. Piro, M. Renzo, C. D. Ott, D. Clausen, S. M. Couch, J. Ellis, and L. F. Roberts, Light Curves of Core-Collapse Supernovae with Substantial Mass Loss using the New Open-Source SuperNova Explosion Code (SNEC), *Astrophys. J.* **814**, 63 (2015).
- [47] Z. Wu, G. Ricigliano, R. Kashyap, A. Perego, and D. Radice, Radiation hydrodynamics modelling of kilonovae with SNEC, *Mon. Not. Roy. Astron. Soc.* **512**, 328 (2022).
- [48] J. Lippuner and L. F. Roberts, SkyNet: A modular nuclear reaction network library, *Astrophys. J. Suppl.* **233**, 18 (2017).
- [49] F. Magistrelli, S. Bernuzzi, A. Perego, and D. Radice, Element Formation in Radiation-hydrodynamics Simulations of Kilonovae, *Astrophys. J. Lett.* **974**, L5 (2024).
- [50] F. Magistrelli, M. Jacobi, S. Bernuzzi, *et al.*, Self-consistent nucleosynthesis and kilonova predictions from radiation-hydrodynamics simulations with coupled nuclear networks, in prep. (2025).
- [51] M. Wiescher *et al.*, The Jina Reaclib Database: its Recent Updates and Impact on Type-i X-ray Bursts, *Astrophys. J. Suppl.* **189**, 240 (2010).
- [52] J. Lippuner and L. F. Roberts, r-Process Lanthanide Production and Heating Rates in Kilonovae, *Astrophys. J.* **815**, 82 (2015).
- [53] A. Perego *et al.*, Production of Very Light Elements and Strontium in the Early Ejecta of Neutron Star Mergers, *Astrophys. J.* **925**, 22 (2022).
- [54] A. Perego, D. Radice, and S. Bernuzzi, AT 2017gfo: An Anisotropic and Three-component Kilonova Counterpart of GW170817, *Astrophys. J. Lett.* **850**, L37 (2017).
- [55] W. E. Kerzendorf and S. A. Sim, A spectral synthesis code for rapid modelling of supernovae, *Mon. Not. Roy. Astron. Soc.* **440**, 387 (2014).
- [56] J. H. Gillanders, S. J. Smartt, S. A. Sim, A. Bauswein, and S. Goriely, Modelling the spectra of the kilonova AT2017gfo – I. The photospheric epochs, *Mon. Not. Roy. Astron. Soc.* **515**, 631 (2022).
- [57] Y. Tarumi, K. Hotokezaka, N. Domoto, and M. Tanaka, Non-LTE analysis for Helium and Strontium lines in the kilonova AT2017gfo, [arXiv:2302.13061 \[astro-ph.HE\]](https://arxiv.org/abs/2302.13061) (2023).
- [58] A. Snepken *et al.*, Helium as an Indicator of the Neutron-Star Merger Remnant Lifetime and its Potential for Equation of State Constraints, [arXiv:2411.03427 \[astro-ph.HE\]](https://arxiv.org/abs/2411.03427) (2024).
- [59] J. Pruet, R. D. Hoffman, S. E. Woosley, H. T. Janka, and R. Buras, Nucleosynthesis in early supernova winds. 2. the role of neutrinos, *Astrophys. J.* **644**, 1028 (2006).
- [60] C. Frohlich, G. Martinez-Pinedo, M. Liebendorfer, F. K. Thielemann, E. Bravo, W. R. Hix, K. Langanke, and N. T. Zinner, Neutrino-induced nucleosynthesis of $a > 64$ nuclei: the nu p-process, *Phys. Rev. Lett.* **96**, 142502 (2006).
- [61] S. Wanajo, The rp-process in neutrino-driven winds, *Astrophys. J.* **647**, 1323 (2006).
- [62] S. Wanajo, B. Müller, H.-T. Janka, and A. Heger, Nucleosynthesis in the Innermost Ejecta of Neutrino-driven Supernova Explosions in Two Dimensions, *Astrophys. J.* **852**, 40 (2018).
- [63] N. Nishimura, T. Rauscher, R. Hirschi, G. Cescutti, A. S. J. Murphy, and C. Fröhlich, Uncertainties in νp -process nucleosynthesis from Monte Carlo variation of reaction rates, *Mon. Not. Roy. Astron. Soc.* **489**, 1379 (2019).
- [64] I. Kullmann, S. Goriely, O. Just, R. Ardevol-Pulpillo, A. Bauswein, and H. T. Janka, Dynamical ejecta of neutron star mergers with nucleonic weak processes I: nucleosynthesis, *Mon. Not. Roy. Astron. Soc.* **510**, 2804 (2022).
- [65] D. Watson *et al.*, Identification of strontium in the merger of two neutron stars, *Nature* **574**, 497 (2019).

- [66] N. Domoto, M. Tanaka, S. Wanajo, and K. Kawaguchi, Signatures of r-process elements in kilonova spectra, *Astrophys. J.* **913**, 26 (2021).
- [67] K. Hotokezaka, S. Wanajo, M. Tanaka, A. Bamba, Y. Terada, and T. Piran, Radioactive decay products in neutron star merger ejecta: heating efficiency and γ -ray emission, *Mon. Not. Roy. Astron. Soc.* **459**, 35 (2016).
- [68] L.-X. Li, Radioactive Gamma-Ray Emissions from Neutron Star Mergers, *Astrophys. J.* **872**, 19 (2019).
- [69] O. Korobkin *et al.*, Gamma-rays from kilonova: a potential probe of r-process nucleosynthesis, *Astrophys. J.* [10.3847/1538-4357/ab64d8](https://doi.org/10.3847/1538-4357/ab64d8) (2020).
- [70] J. A. Tomsick *et al.*, The Compton Spectrometer and Imager, *PoS ICRC2023*, 745 (2023).
- [71] M. Tavani *et al.* (e-ASTROGAM), Science with e-ASTROGAM: A space mission for MeV–GeV gamma-ray astrophysics, *JHEAp* **19**, 1 (2018).
- [72] T. Shutt *et al.*, The GammaTPC Gamma-Ray Telescope Concept, [arXiv:2502.14841 \[astro-ph.IM\]](https://arxiv.org/abs/2502.14841) (2025).
- [73] K. Maguire *et al.*, Using late-time optical and near-infrared spectra to constrain Type Ia supernova explosion properties, *Mon. Not. Roy. Astron. Soc.* **477**, 3567 (2018).
- [74] Q. Pognan, J. Grumer, A. Jerkstrand, and S. Wanajo, NLTE spectra of kilonovae, *Mon. Not. Roy. Astron. Soc.* **526**, 5220 (2023), [Erratum: *Mon. Not. Roy. Astron. Soc.* 537, 1093–1098 (2025)].
- [75] C. Musolino, L. Rezzolla, and E. R. Most, On the impact of neutrinos on the launching of relativistic jets from "magnetars" produced in neutron-star mergers, [arXiv:2410.06253 \[astro-ph.HE\]](https://arxiv.org/abs/2410.06253) (2024).